

# Lutetium oxyorthosilicate (LSO) intrinsic activity correction and minimal detectable target activity study for SPECT imaging with a LSO-based animal PET scanner

Rutao Yao<sup>1</sup>, Tianyu Ma<sup>1,2</sup> and Yiping Shao<sup>1,3</sup>

<sup>1</sup> Department of Nuclear Medicine, State University of New York at Buffalo, Buffalo, New York 14214, USA

<sup>2</sup> Department of Engineering Physics, Tsinghua University, Beijing, People's Republic of China

<sup>3</sup> Department of Imaging Physics, University of Texas M.D. Anderson Cancer Center, Texas, USA

E-mail: [rutaoyao@buffalo.edu](mailto:rutaoyao@buffalo.edu)

Received 25 March 2008, in final form 23 May 2008

Published 30 July 2008

Online at [stacks.iop.org/PMB/53/4399](http://stacks.iop.org/PMB/53/4399)

## Abstract

This work is part of a feasibility study to develop SPECT imaging capability on a lutetium oxyorthosilicate (LSO) based animal PET system. The SPECT acquisition was enabled by inserting a collimator assembly inside the detector ring and acquiring data in singles mode. The same LSO detectors were used for both PET and SPECT imaging. The intrinsic radioactivity of <sup>176</sup>Lu in the LSO crystals, however, contaminates the SPECT data, and can generate image artifacts and introduce quantification error. The objectives of this study were to evaluate the effectiveness of a LSO background subtraction method, and to estimate the minimal detectable target activity (MDTA) of image object for SPECT imaging. For LSO background correction, the LSO contribution in an image study was estimated based on a pre-measured long LSO background scan and subtracted prior to the image reconstruction. The MDTA was estimated in two ways. The empirical MDTA (eMDTA) was estimated from screening the tomographic images at different activity levels. The calculated MDTA (cMDTA) was estimated from using a formula based on applying a modified Currie equation on an average projection dataset. Two simulated and two experimental phantoms with different object activity distributions and levels were used in this study. The results showed that LSO background adds concentric ring artifacts to the reconstructed image, and the simple subtraction method can effectively remove these artifacts—the effect of the correction was more visible when the object activity level was near or above the eMDTA. For the four phantoms studied, the cMDTA was consistently about five times of the corresponding eMDTA. In summary, we implemented a simple LSO background subtraction method and demonstrated its effectiveness.

The projection-based calculation formula yielded MDTA results that closely correlate with that obtained empirically and may have predicative value for imaging applications.

(Some figures in this article are in colour only in the electronic version)

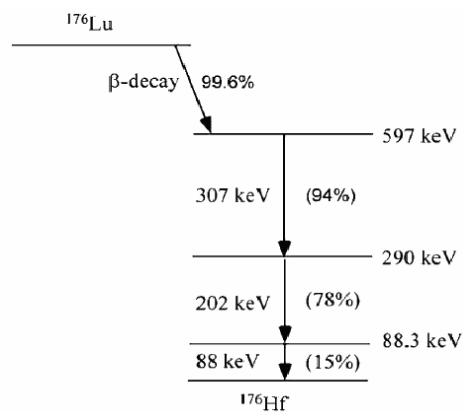
## 1. Introduction

Animal SPECT is a molecular imaging instrument that has become increasingly important in biomedical research (Meikle *et al* 2005). It has the advantages of accessing a large established library of radiotracers, low cost with radiotracer production and relatively long half-lives which can benefit tracer transportation and studies with long biological time span. Recently, the strikingly high resolution and significantly improved sensitivity achieved with a new multiple pinhole collimator design (Schramm *et al* 2003, Beekman and Van Der Have 2007) has demonstrated great potentials in animal SPECT systems. One major limiting factor for the wide acceptance of the animal SPECT system, similar to other nuclear imaging systems, is its significant cost. While the installed animal PET base is about triple the size of animal SPECT (Frost and Sullivan 2006), our group has proposed to develop a technology that enables SPECT imaging on an existing animal PET (Yao *et al* 2006, Ma *et al* 2007b, Shao *et al* 2006). The primary advantage of this concept is that the existing animal PET owners will have the option of accessing an animal SPECT system with much lower cost than a dedicated system. In addition, the dual-function imaging system provides a platform for investigating PET-SPECT dual tracer imaging applications (Shao *et al* 2007, Ma *et al* 2007a).

As compared to dedicated animal SPECT scanners, the first challenge for this development is the limited space within the animal PET gantry. The imaging field of view (FOV) and the magnification factor, assuming pinhole or similar collimator is used, need to be carefully balanced to obtain a high performance and practical system. In addition, there will be no room for using a transmission source to conduct SPECT-based attenuation correction. However, the attenuation correction mechanism designed for PET (Lehnert *et al* 2006) may be used for SPECT imaging. The second challenge is that the PET detectors have lower energy resolution than that of dedicated SPECT scanners and therefore there will be more scattered events. This may not be a serious issue if only small animals such as rats and mice are the targeted imaging subjects. The third challenge is the LSO crystal's intrinsic activity, if the animal PET scanner uses LSO crystal detectors. This subject is the main focus of this paper.

Due to its short decay time, high stopping power and light output, LSO scintillator has been the crystal of choice for making PET scanners. A significant number of clinical PET systems and most of the pre-clinical PET scanners in service use LSO as the detector crystal. One drawback of the LSO crystal, however, is that a fraction of lutetium,  $^{176}\text{Lu}$  (2.6% abundance), is a natural radioactive element and has very long half-life ( $\sim 3.8 \times 10^{10}$  years). Figure 1 shows a simplified decay scheme of  $^{176}\text{Lu}$ . The energies of main gamma rays emitted from this nuclide are 307, 202 and 88 keV. The total LSO intrinsic activity for the micro-PET Focus 120 system is estimated to be 5.1  $\mu\text{Ci}$ , or 13.7 Bq/crystal.

The intrinsic LSO activity has only minor impacts on PET imaging performance due to the relative low energy of gamma emissions, PET system's high-energy threshold and high sensitivity (Watson *et al* 2004, Goertzen *et al* 2007), and coincidence acquisition. However, this intrinsic background activity may have serious impacts on SPECT imaging based on using LSO PET detectors, since the energy range of LSO gamma emissions overlaps with



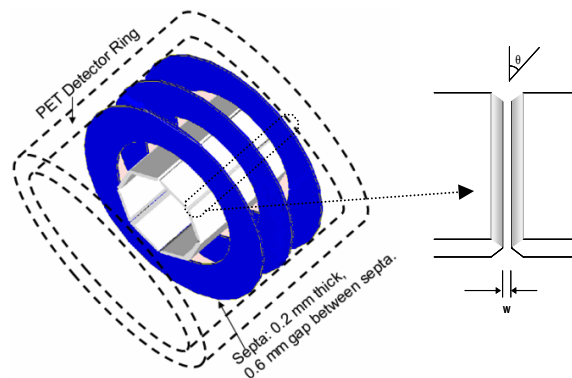
**Figure 1.** A simplified decay scheme of  $^{176}\text{Lu}$  showing the cascade of prompt gamma emissions. The intensity of each type of emission is in relative to the decay of  $^{176}\text{Lu}$ .

that used in SPECT imaging, and the sensitivity of this SPECT system is low for detecting photons from imaging objects due to the presence of the collimator but high ( $\sim 100\%$ ) for LSO background activities. For optimal SPECT imaging performance, the contributions from the LSO background activity need to be removed with minimal artifacts.

Since intrinsic LSO activity is independent of object activity, it can be pre-measured and then subtracted from the total projection data acquired in each study. To minimize the statistical noise introduced by the subtraction, the LSO background in a study was estimated from a pre-measured long acquisition of a background dataset by scaling down to the acquisition time of the study. While the correction method is straightforward, the effects of the LSO background activity on radiation dose and acquisition time requirement for obtaining good image quality are not clear.

Intuitively, the reconstructed image quality depends strongly on the relative weight of signal and noise in projection data. From an imaging point of view, one important value to know for imaging studies is the minimal detectable target activity (MDTA) level, the level of object activity above which the acquired projection data can yield an image with a visible target pattern and without noticeable artifacts. With the additional LSO intrinsic background activity, the MDTA level will be higher for the LSO-based SPECT system as compared to typical SPECT systems which do not have crystal intrinsic activity. Many researchers have studied the image formation process and noise propagation theory (Budinger *et al* 1978, Huesman 1984, Barrett *et al* 1994, Wilson *et al* 1994, Qi and Huesman 2006), but there is not a general formula to estimate the MDTA level, which can be very useful in predicting the feasibility of an image study or guiding the design of the imaging protocol.

In this work, we report LSO background activity's presentation in SPECT images, the implementation of a LSO background activity correction method and the effect of applying the correction method on image. To provide a simple way to assess target detectability in general imaging applications which may have different activity distributions, we designed a projection-data-based MDTA estimation formula to calculate cMDTA. The validity of the formula was assessed by comparing the cMDTA with the eMDTA obtained empirically from screening Monte Carlo simulated and real experimental tomographic images at different activity levels. While the result from a real experiment was the gold standard, Monte Carlo simulation was used for its flexibility in producing desired activity distribution and intensity levels.



**Figure 2.** The drawing on the left shows the collimator insert in the PET. One of eight slit apertures is shown on the right. The slit open angle  $\theta$  and aperture width  $w$  were  $45^\circ$  and 0.6 mm, respectively. The inner (opening) and outer diameters of the septa were 84 and 132 mm, respectively.

## 2. Materials and methods

### 2.1. Animal PET scanner and collimator insert

A microPET Focus 120<sup>TM</sup> (Siemens Preclinical Solutions, Knoxville, TN) scanner (Laforest *et al* 2007) was used for developing the SPECT imaging capability (Shao *et al* 2006, Yao *et al* 2006, Ma *et al* 2007b). The scanner consists of 96 detector blocks arranged in four rings. Each block is composed of  $12 \times 12$  LSO crystals. A slit-slat collimator was inserted in the PET gantry for SPECT imaging, as illustrated in figure 2. The collimator consisted of eight slits and 21 annular septa. The slit plates were 2.5 mm thick lead and were aligned to the axial direction of the PET scanner. The septa were 0.2 mm thick tungsten, and were spaced evenly (0.6 mm apart) along the axial direction outside the slit plates. This configuration produced a two-dimensional (2D) fan-beam collimation geometry. The radius of slit apertures was 30 mm and the open-angle of the aperture was  $45^\circ$ . This setup provided a 4 cm diameter transverse field of view (FOV).

The system sensitivity obtained from Monte Carlo simulation (Santin *et al* 2003) of a line source placed in the center of the FOV was 0.022% and 0.006% with energy windows of 120–160 keV and 135–145 keV, respectively. The system sensitivity is proportional to the number of slit apertures. Knowing that the energy spectrum of the LSO intrinsic activity was nearly flat across a wide energy range (Goertzen *et al* 2007), a fixed energy window, 135–145 keV was used in all studies to minimize the scatter effects. As the sensitivity variation over the FOV was small ( $<10\%$ ), we used the value 0.006% as the average system sensitivity for all locations across FOV to simplify the projection-data-based MDTA derivation in section 2.4. In the following contexts, the average system sensitivity for the detector area opening to one slit aperture is noted as  $\text{Sen}_{\text{slit}}$ , which is 1/8th of the system sensitivity with eight slits.

### 2.2. System normalization and image reconstruction

The sensitivity coefficients of crystals were obtained from scanning a uniform cylinder phantom (1.4 cm diameter, 9 cm long) filled with 1.3 mCi  $^{99\text{m}}\text{Tc}$  solution. Without the

collimator insert, the cylinder was scanned for 5 min with an energy window of 135–145 keV. The average total count per crystal was about 50 000. The normalization coefficients were applied to the projection data pre-corrected for LSO background and radioactive decay before image reconstruction. Due to the small size of the targeted imaging objects, such as rats and mice, scatter and attenuation were not implemented in this work.

An iterative reconstruction program with an ordered subset expectation maximization (OSEM) algorithm was used for all the image reconstruction tasks (Yao *et al* 2006, Ma *et al* 2007b). The number of iterations and subsets, 10 and 8 respectively, was empirically determined to give the optimal results. The reconstructed image voxel size was 0.25 mm × 0.25 mm × 1.6 mm. The slice thickness 1.6 mm, which matches the crystal ring height, was selected for facilitating the cMDTA formula derivation in section 2.4.

### 2.3. Correction of LSO background activity

A 24 h LSO background activity was measured and statistically replicated for 60 times to act as multiple projections, and reconstructed to study the pattern from the mean of LSO intrinsic activity. The noise contributed by the LSO activity shall have the same pattern as being described by Wilson and Tsui (1993).

The 24 h LSO background measurement was also used as the noise-free dataset for estimating the LSO background counts in individual studies. The estimation was simply to scale the crystal's counts of the 24 h dataset down to the imaging acquisition time of a specific study.

In an arbitrary crystal of a projection view dataset for SPECT imaging, assuming the actual and estimated LSO background counts as  $N_{\text{LSO}}$  and  $\hat{N}_{\text{LSO}}$ , respectively, the contribution of the LSO background to the total detected counts  $N_d$  can be corrected by subtraction, i.e.

$$N_o = N_d - \hat{N}_{\text{LSO}}, \quad (1)$$

where  $N_o$  is the net detected counts in the crystal from the imaging object.

### 2.4. cMDTA based on projection data for SPECT imaging

In order to derive the cMDTA formula based on the signal detectability in a projection dataset, we start by reviewing the derivation of the Currie equation as described in textbook (Knoll 2000, pp 94–6).

**2.4.1. Currie equation.** Use the symbols introduced in (1), and assume that  $N_{\text{LSO}}$  is acquired from a separate LSO background activity measurement with same acquisition time, the LSO background corrected signal counts are

$$N_o = N_d - N_{\text{LSO}}. \quad (2)$$

Since  $N_d$  and  $N_{\text{LSO}}$  are independent entities following Poisson distribution, the noise in  $N_o$  is

$$\sigma_{N_o} = \sqrt{\sigma_{N_d}^2 + \sigma_{N_{\text{LSO}}}^2} = \sqrt{N_d + N_{\text{LSO}}} = \sqrt{2N_{\text{LSO}} + N_o}. \quad (3)$$

Expand for  $N_o \ll N_{\text{LSO}}$ ,

$$\sigma_{N_o} \approx \sqrt{2N_{\text{LSO}}} \left( 1 + \frac{N_o}{4N_{\text{LSO}}} \right). \quad (4)$$

If we ignore the small value  $\frac{N_o}{4N_{\text{LSO}}}$ ,

$$\sigma_{N_o} \approx \sqrt{2N_{\text{LSO}}}. \quad (5)$$

The minimal detectable level of  $N_o$  that above which the false-positive probability is 5% or less, and below which the false-negative probability is less than 5%, noted as  $MDN_o$ , is (Knoll 2000)

$$MDN_o = L_C + 1.645 \cdot \sigma_{N_o}, \quad (6)$$

where  $L_C = 1.645\sigma_{N_o}$ , known as the critical level.

Replace the  $L_C = 1.645\sigma_{N_o}$  and  $\sigma_{N_o} = \sqrt{2N_{LSO}}$  in (6),

$$MDN_o \approx 1.645\sqrt{2N_{LSO}} + 1.645\sqrt{2N_{LSO}} = 4.653\sqrt{N_{LSO}}. \quad (7)$$

If the term  $\frac{N_o}{4N_{LSO}}$  in (4) is not ignored, we can use the result of (7) to replace  $N_o$  in (4), then

$$MDN_o = 4.653\sqrt{N_{LSO}} + 2.706. \quad (8)$$

This is the Currie equation.

**2.4.2. Modified Currie equation.** With the statistical noise-free estimate of the intrinsic activity counts,  $\hat{N}_{LSO}$ , for LSO background correction,  $N_o = N_d - \hat{N}_{LSO}$ , and  $\sigma_{\hat{N}_{LSO}} = 0$ .

The noise in the net signal  $N_o$  is

$$\sigma_{N_o} = \sqrt{\sigma_{N_d}^2 + \sigma_{\hat{N}_{LSO}}^2} = \sqrt{N_{LSO} + N_o} = \sqrt{N_{LSO}} \left( 1 + \frac{N_o}{2N_{LSO}} \right). \quad (9)$$

Follow the same steps of Currie equation derivation, we have

$$MDN_o = 3.29\sigma_{N_{LSO}} + 2.706 = 3.29\sqrt{N_{LSO}} + 2.706. \quad (10)$$

**2.4.3. The cMDTA for a thin line-source target.** To facilitate the derivation of the cMDTA formula, we consider the slit-slat collimator setup form an ideal 2D collimation in the planes defined by septa. That is, the variation of source distribution and detection sensitivity along axial direction is ignored. The axial height of the 2D plane we study is the height of one crystal ring (1.6 mm). Figure 3 shows a transverse sectional view of the collimator and detector setup in the 2D plane.

For a slit aperture and a line source (along axial direction) in the FOV, there may be several crystals facing the slit aperture that will detect the events from the source. When the transverse sizes of both the line source and the aperture opening are small enough, there will be only one crystal that detects the line source, as illustrated in figure 3. At the same time, this crystal also collects counts from its LSO background activity.

Assuming the acquisition time for the projection is  $T$  s, the counts from intrinsic LSO activity in the crystal is

$$N_{LSO} = T \cdot A_{LSO}, \quad (11)$$

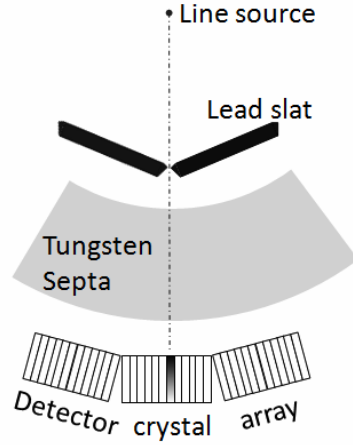
where  $A_{LSO}$  is the LSO intrinsic activity in the crystal, with the unit of Becquerel (Bq). It was 0.042 Bq for crystals in the middle of detector blocks.

The counts contributed by the line source to the crystal are

$$N_o = A_{\text{line}} \cdot T \cdot \text{Sen}_{\text{crystal}}, \quad (12)$$

where  $A_{\text{line}}$  is the activity of the line source in a length equal to one crystal height,  $\text{Sen}_{\text{crystal}}$  is the sensitivity of the crystal to the line source.

The line source used in simulation for deriving system sensitivity was 0.2 mm in diameter and was placed at the center FOV. The width of the line-source projection on the detector crystal was 0.28 mm, less than the width of one crystal (1.6 mm). So the system sensitivity



**Figure 3.** A transverse sectional view of the slit-slat collimator and detector setup for the SPECT imaging system. The thin line source was only detected by the shaded detector crystal.

of one slit aperture (see section 2.1) is equal to the crystal's sensitivity to the line source,  $\text{Sen}_{\text{crystal}}$ , i.e.

$$\text{Sen}_{\text{crystal}} = \text{Sen}_{\text{slit}} = 6 \times 10^{-5} / 8 = 7.5 \times 10^{-6}.$$

We hypothesize that for the line source to be visible in the reconstructed image, the number of events detected in the crystal that exposes to the source in a projection must be above the MDN level as calculated in (10). Therefore, combine (10), (11) and (12), the activity in the line source is

$$A_{\text{line}} = \frac{\text{MDN}_{\text{line}}}{T \cdot \text{Sen}_{\text{slit}}} = \frac{(3.29 \cdot \sqrt{T \cdot A_{\text{LSO}}} + 2.706)}{T \cdot \text{Sen}_{\text{slit}}}. \quad (13)$$

$A_{\text{line}}$  here is the cMDTA for the line source.

**2.4.4. cMDTA— the target has certain size.** Equation (13) calculates the cMDTA of a thin line source. In this paragraph, we consider a circular target region with uniform activity distribution. If the target is located at the center of FOV (CFOV), the activity will be equally projected to  $n$  consecutive crystals in all projections, and the magnification factor  $m$  at CFOV, which is  $\sim 1.4$  for the collimator configuration described in section 2.1, can be used to calculate the projection span:

$$n = D_{\text{target}} \cdot \frac{m}{\text{crystal\_width}}, \quad (14)$$

where the  $\text{crystal\_width}$  is the crystal size in the tangential direction. It is 1.6 mm for the animal PET scanner we used.  $D_{\text{target}}$  is the diameter of the target. When the target is off-centered, the projection span  $n$  and the magnification factor  $m$  vary over different projections. In this work, we use the  $n$  and  $m$  values in CFOV as an averaged estimation over all the tomographic projections. On average, each crystal detects  $1/n$  of target's total projection counts. Expand (13) for this situation,

$$\text{cMDTA}_{\text{target}/n} = \frac{(3.29 \sqrt{T \cdot A_{\text{LSO}}} + 2.706)}{T \cdot \text{Sen}_{\text{slit}}}.$$

Rearranging, we have

$$\text{cMDTA}_{\text{target}} = \frac{n \cdot (3.29\sqrt{T \cdot A_{\text{LSO}}} + 2.706)}{T \cdot \text{Sen}_{\text{slit}}}. \quad (15)$$

*2.4.5. cMDTA—the target has a surrounding background activity.* The target selected in the derivation of (15) does not have surrounding object-background activity except the LSO activity. For an object with surrounding background activity  $A_{\text{bkg}}$ , the number of events from this region and collected in the crystal detecting the target is

$$N_{\text{bkg}} = A_{\text{bkg}} \cdot T \cdot \text{Sen}_{\text{slit}}/n_{\text{bkg}}, \quad (16)$$

where  $n_{\text{bkg}}$  is the number of crystals exposed to the image object background region.

Now for the signal of the target to be detectable, it must overcome both the LSO activity and object background in the projection, therefore,

$$\text{MDN}_{\text{target}} = 3.29 \cdot \sqrt{N_{\text{LSO}} + N_{\text{bkg}}} + 2.706. \quad (17)$$

For the cMDTA in the target is calculated same as (13),

$$\text{cMDTA} = \frac{n \cdot \text{MDN}_{\text{target}}}{T \cdot \text{Sen}_{\text{slit}}} = \frac{(3.29\sqrt{T \cdot A_{\text{LSO}} + N_{\text{bkg}}} + 2.706)}{T \cdot \text{Sen}_{\text{slit}}}. \quad (18)$$

## 2.5. Phantom studies

Four phantoms with different activity distribution, activity level and acquisition time were studied for evaluating the LSO correction method and obtaining the eMDTA. eMDTA is useful for understanding the imaging system's capability and also serves the purpose of assessing the validity of the cMDTA calculation formula.

The Monte Carlo simulation package, GATE 3.0 (Jan *et al* 2004), was used for emulating photon propagation and detection processes of the virtual scanner with the exact collimator and detector configuration. Simulation settings were made to ensure the highest resemblance of the virtual scanner and the real system. The simulation tasks were distributed to multiple computer nodes on a Linux cluster with random seeds pre-generated and saved in a file. The simulation results generated on multiple compute nodes were collected and analyzed.

*2.5.1. Experimental hot-rod phantom.* We used an ultra-micro hot-rod phantom (Data Spectrum Inc., Hillsborough, NC) to study the effects of LSO intrinsic activity correction and acquisition time on image quality. The phantom was filled with a total of 1116  $\mu\text{Ci}$   $^{99\text{m}}\text{Tc}$  solution. The activity in the hot-rod section per crystal ring was 9  $\mu\text{Ci}$ . It was rotated for 120 steps at  $3^\circ/\text{step}$ , and scanned for 128 s at each step. To estimate the MDTA empirically, the acquired listmode data were also used to extract four additional studies that were equivalent to 11, 21, 53, and 84 s scan time per projection and with the same number of projections. The scan time was selected empirically to screen the eMDTA level.

*2.5.2. Simulated hot-rod phantom with cold background.* We simulated the ultra-micro hot-rod phantom (10 mm height, uniform hot-rod pattern throughout the axial direction) that had 5000, 500, 200, 114, 80, 50, 20 and 10  $\mu\text{Ci}$  activity per crystal ring. The phantom was scanned for  $120 \times 12$  s projections. The 24 h LSO intrinsic activity template was scaled to 12 s and was added with Poisson noise to introduce the LSO intrinsic background activity to the simulated phantom projection data. The 12 s scaled-down LSO template was also used for crystal intrinsic activity correction.





**Figure 4.** A diagram illustrating the composition of the contrast phantom. The small black and white cylinders were filled with  $^{99m}\text{Tc}$  solution and water, respectively. The main cylinder was filled with background activity.

**2.5.3. Simulated hot-rod phantom with warm background.** A modified hot-rod phantom with a ‘warm’ instead of completely ‘cold’ background was simulated. In this phantom, the activity concentration in hot rods was four times that in the ‘warm’ region. The height of the phantom was 10 mm. Eight activity levels in the phantom were studied: 5000, 500, 200, 114, 80, 50, 40, 20 and 10  $\mu\text{Ci}$  activity per crystal ring. Each phantom was scanned for 12 s per projection for 120 projections. The 20 and 40  $\mu\text{Ci}$  activity levels were also simulated for 24 and 60 s projection acquisition times.

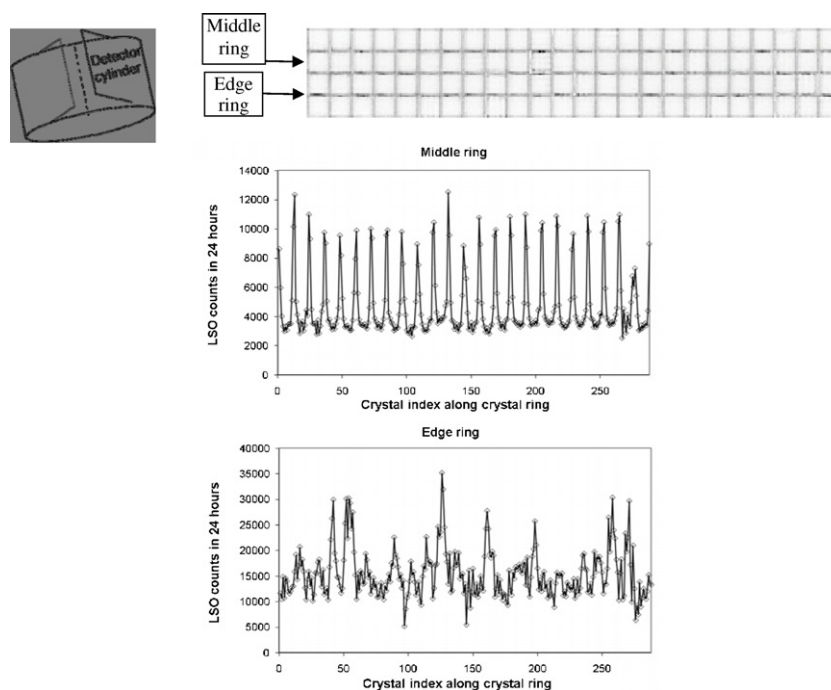
**2.5.4. Experimental contrast phantom.** We assembled a contrast phantom that was composed of a main cylinder (2.8 cm diameter, 2.8 cm in height), with two small cylinder chambers (1.43 cc each, 8 mm diameter) inside. One chamber was filled with water and the other with 84  $\mu\text{Ci}$   $^{99m}\text{Tc}$  solutions. The rest of the main cylinder was filled with 254  $\mu\text{Ci}$  activity in 10.6 cc volume. So the activity concentration in the hot chamber was 2.5 times that in the main cylinder. Figure 4 shows a diagram of the phantom. Three scans were acquired in 12, 24 and 60 s per projection,  $6^\circ$  per incremental angle, and for 60 total projections.

## 2.6. Assessment of target detectability

Two methods were used for the assessment of the target detectability in a reconstructed image. For the hot-rod phantoms, we used visual inspection to judge whether the rod pattern in the 1.35 mm section was distinguishable in the reconstructed images. When the pattern was distinguishable, we considered that the target (1.35 mm rod) was detectable. The 1.35 mm rod section was selected as it is the resolution limit of the SPECT system and it is most sensitive for the assessment. For the contrast phantom studies, the image quality was quantified with the signal-noise ratio (SNR),

$$\text{SNR} = \frac{\text{mean}_{\text{hot\_ROI}} - \text{mean}_{\text{cold\_ROI}}}{\sqrt{(\text{var}_{\text{hot\_ROI}} + \text{var}_{\text{cold\_ROI}})}}, \quad (19)$$

where the hot\_ROI and cold\_ROI are hot and cold regions defined in the images.



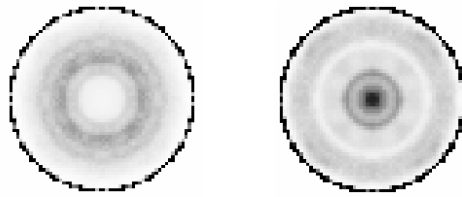
**Figure 5.** The LSO activity distribution over the detector crystal array of the animal PET scanner is shown in the top row image. The graphs in the second and third rows are the section profiles of the intrinsic activity map of the crystal rings in the middle and edge of detector blocks, respectively.

### 3. Results

#### 3.1. LSO intrinsic activity in projection data

The image in the top row of figure 5 shows the LSO intrinsic activity distribution over the scanner's detector crystal map. The drawing on the left-side of the first row shows that the detector crystal map is the unfolded form of the detector cylinder. The vertical direction of the image aligns to the detector cylinder's axial axis. There are four detector blocks, or 48 crystals along the axial direction. Each row of the image corresponds to a ring of crystals. The activity distribution was acquired for 24 h with the 135–145 keV energy window. The reversed black-on-white linear palette was used for displaying images. This palette was also used throughout this paper. The distribution had a grid pattern with each detector block being a grid element. The grid pattern reveals that the LSO activity of the edge crystal is different from that of the middle crystals of each detector block.

The section profiles of crystals in a selected middle and edge of detector block, as indicated by the arrows in the first row, are shown by the graphs in the 2nd and 3rd rows of figure 5, respectively. The dark grid lines correspond to the edge LSO crystals of detector blocks, where higher energy (outside the 135–145 keV window) gamma rays from  $^{176}\text{Lu}$  lose energy through Compton interactions and deposit part of their energy (in the 135–145 keV window) in the crystals. The crystals in the center of the block have more chances to collect the full energy instead, and therefore have less high-energy photon contributions in the 135–145 keV energy window. With the 135–145 keV energy window, activities of the crystals at the edge



**Figure 6.** The two transverse view images were reconstructed from high count LSO intrinsic activity measurement. Respectively, the left and right images were from a ring of crystals at the middle and edge of a detector block in the axial direction.

of the detector blocks were about 0.125 Bq. The average activity of the crystals in the middle of the detector blocks was 0.042 Bq (Bq)/crystal, noted as  $A_{\text{LSO}}$  in the rest of the contexts.

### 3.2. The image pattern of the LSO intrinsic activity




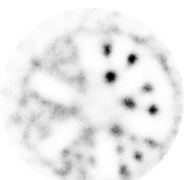

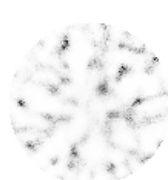
The image reconstructed from the 24 h LSO intrinsic activity measurement is shown in figure 6. The LSO activity formed concentric rings in tomographic images. The variation of LSO intrinsic activity over detector crystal locations caused different patterns in the transverse view images. With an effective correction method, the mean value of the intrinsic activity can be removed. However, its noise will remain and contribute to the reconstructed images in the same pattern (Wilson and Tsui 1993). Figure 6 provides a hint for identifying the LSO activity effect on reconstructed images.

Because of the different levels of LSO activity in the middle and edge crystal rings of a detector block in the axial direction, the MDTA levels for the corresponding planes will be different. However, the same principle, such as that we developed in the cMDTA calculation method in section 2.4, applies to both levels. For simplicity and without affecting the outcome of this investigation, we evaluated only the planes formed by crystal rings in the middle of detector blocks in the following phantom studies.

### 3.3. Experimental hot-rod phantom

The improvement of image quality with the LSO intrinsic activity correction method is clearly demonstrated by the experimental hot-rod phantom study, as shown in figure 7. The ring artifacts seen in the images without LSO activity correction disappeared in the images with correction applied. This effect is clear at all the measurement statistical levels shown. In figure 7, the three count levels were obtained by using same activity configuration but different acquisition time per projection. The activity levels reported are the activity in one 1.35 mm diameter hot rod with the height of one crystal ring. The clear improvement of image quality with the images shown in the right column (LSO activity corrected) was due partially to the application of crystal sensitivity normalization, while the simulated system had perfect crystal sensitivity uniformity and did not have this factor (perfectly uniform crystal sensitivity simulated).

The three count levels shown were selected to represent three conditions that we are interested in: (1) the high activity level that the LSO intrinsic activity had minor effects; (2) the lowest activity level that still allowed identifying the 1.35 mm hot-rod pattern in the reconstructed image; and (3) the highest activity level at which the 1.35 mm hot-rod pattern in the reconstructed image was unidentifiable. The maximum value of the color palette for

| Activity (cMDTA) $\mu\text{Ci}$ in a<br>1.35 mm hot-rod, Acq.<br>Time/projection | $A_{LSO}$ uncorrected  | $A_{LSO}$ corrected  |
|--|--|--|
| 0.18 (0.36) $\mu\text{Ci}$ , 120 sec.  |   |   |
| 0.18 (0.61) $\mu\text{Ci}$ , 53 sec.   |   |   |
| 0.18 (1.7) $\mu\text{Ci}$ , 21 sec.  |  |  |

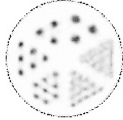
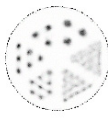
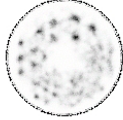
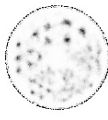
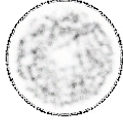
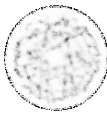
**Figure 7.** The images of the hot-rod experimental phantom at three representative acquisition times. The LSO intrinsic activity correction clearly improved image quality. The hot-rod diameters in the six sections were 2.4, 2.0, 1.7, 1.35, 1.0 and 0.75 mm, respectively. The distance between hot rods in each section was twice that of the hot-rod diameter in the section. The two other hot-rod phantoms have the same sizes.

each image was proportional to its activity level for fair visual comparison. For other phantom studies reported in this work, similar considerations about selecting the representative count level (activity or acquisition time) and making color palette adjustment were applied.

#### 3.4. Simulated hot-rod phantom with cold background

The images of the ultra-micro hot-rod phantom with *cold background* at three activity levels are shown in figure 8. The acquisition time per projection was fixed at 12 s. With high activity level in the phantom, e.g. 2.26  $\mu\text{Ci}$  in the 1.35 mm diameter hot rod, the multiple concentric ring artifacts from LSO intrinsic activity were not visible. The two lower activity level images without LSO correction showed more ring artifacts. With the LSO activity correction, the image with activity level above MDTA, i.e. the 1.35 mm hot-rod pattern is visible, showed reduced ring artifacts.

An artificial ring is clearly seen in all the three activity level images and relatively more prominent in the two lower activity level images. A simple calculation reveals that this ring

| Activity (cMDTA) $\mu\text{Ci}$<br>in a 1.35 hot-rod | $A_{\text{LSO}}$ Uncorrected  | $A_{\text{LSO}}$ Corrected  |
|--|---|---|
| 2.26 (1.79)  |  |  |
| 0.40 (1.79)  |  |  |
| 0.20 (1.79)  |  |  |

**Figure 8.** The images of a simulated hot-rod cold-background phantom at three activity levels, with and without LSO intrinsic activity correction. The calculated cMDTA was  $1.79 \mu\text{Ci}$  in the 1.35 hot rod.

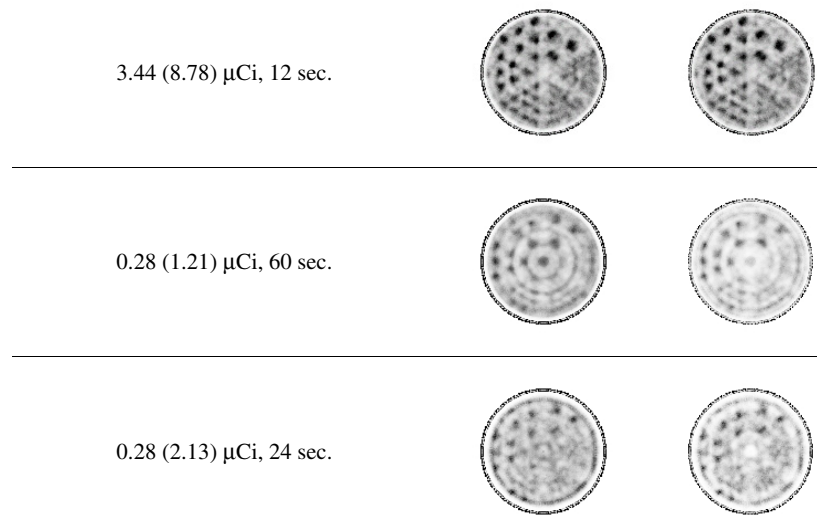
corresponds to the vertical grid lines shown in the LSO distribution map in figure 5. Due to the higher LSO background in these crystal columns, their effect can only be overcome by higher object activity. The images at two lower levels had contrary results in visualizing the 1.35 mm hot-rod pattern, indicating the MDTA, the threshold that decided the target detectability, existed between these two levels.

### 3.5. Simulated hot-rod phantom with warm background

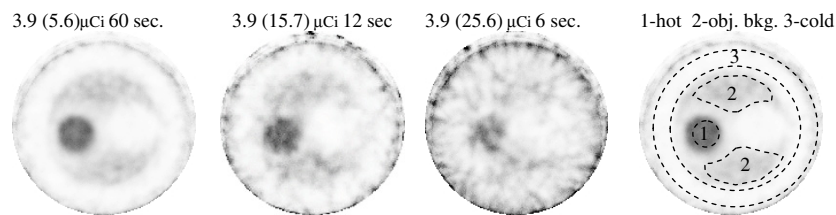
The images of the warm-background hot-rod phantom at three activity levels are shown in figure 9. By design, the imaging object's background activity was proportional to the total activity. So the cMDTA calculated according to (18) increased as the total activity level rose. As a result, the images for all activity levels showed reduced contrast as compared to figure 8. The ring artifacts are present for the images at all the three count levels and were reduced with the LSO background activity correction. It may be due to the uniform crystal sensitivity with simulated data, the effect of intrinsic activity correction was not as visually significant as the experimental results (figure 7).

### 3.6. Experimental contrast and hot-rod phantoms

The images of the experimental contrast phantom at three projection acquisition times, and with LSO activity correction applied, are shown in figure 10. To quantify the image quality, the SNR values for the three images were calculated from those reported in table 1. The hot, object background and cold region of interests (ROI) were manually defined and labeled as 1, 2, 3 respectively in the image shown in the right-most column of the figure. The SNR values for the hot-cold and hot-background ROIs are shown in table 1. By using  $\text{SNR} = 2$  as the threshold for deciding if the expected image pattern is visible, the images reconstructed



**Figure 9.** The images of the ultra-micro hot-rod phantom warm background at three activity levels, with and without LSO intrinsic activity correction. The activity in a 1.35 mm diameter hot-rod and corresponding calculated cMDTA levels, in parenthesis, are also shown. The geometry parameters of the phantom were the same as that in figure 8.

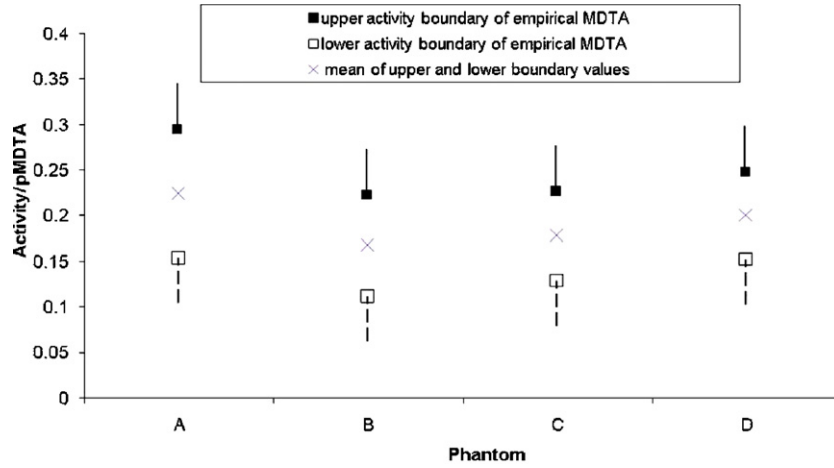


**Figure 10.** Three representative images of the contrast phantom with different acquisition time per projection. The activity in the hot ROI (the target), the calculated cMDTA levels (in parenthesis) and the acquisition times per projection are shown for each image. The ROIs used for calculating the SNR values are overlaid on an image from a high count dataset and are shown in the right-most column.

**Table 1.** The SNRs calculated from the hot and cold ROIs ( $\text{SNR}_{\text{Hot,Cold}}$ ), and the hot and background ROIs ( $\text{SNR}_{\text{Hot,Bkg}}$ ).

| Acq. time (s) | $\text{SNR}_{\text{Hot,Cold}}$ | $\text{SNR}_{\text{Hot,Bkg}}$ |
|---------------|--------------------------------|-------------------------------|
| 60 s          | 5.68                           | 4.04                          |
| 12 s          | 3.46                           | 2.58                          |
| 6 s           | 1.36                           | 1.59                          |

from 12 and 6 s acquisition time per projections were considered to be visible and invisible, respectively.



**Figure 11.** The ratios of eMDTA boundary numbers to calculated cMDTA for (A) experimental hot-rod cold-background phantom; (B) simulated hot-rod, cold-background phantom; (C) simulated hot-rod, warm-background phantom; and (D) experimental contrast phantom.

### 3.7. Comparison of the empirically derived and formula calculated MDTA

The eMDTA is the level between the minimal level that produced the target image and the maximum level that failed to yield the target image. So it can be represented by the upper and lower limits of the range that it is in. Comparing to the phantom studies reported in figures 7–10, the cMDTA levels calculated with (14) and (17) did not directly match the eMDTAs. To seek the connection between the two sets of values, we evaluated the ratio of eMDTA and cMDTA—the eMDTA values were represented by the upper and lower limit levels. The results are summarized in figure 11. For the four phantoms studied, if the mean of the eMDTA upper and lower limit values was used as the eMDTA, the ratio of eMDTA to calculated cMDTA varied from 0.17 to 0.22, with a mean of 0.19 and a standard deviation of 0.03. This indicates close correlation between the two MDTA values.

## 4. Discussions

For an imaging system using detector crystals without intrinsic activity, in (3)  $N_{\text{LSO}} = 0$ , and  $\sigma_0 = \sqrt{N_0}$ . Replacing  $\sigma_0$  in (6), we have  $\text{MDN}_0 = 3.29\sqrt{N_0}$ . It is smaller than the  $\text{MDN}_0 = 3.29\sqrt{N_{\text{LSO}} + N_0}$ , which is the original form of (1) before expanding for  $N_{\text{LSO}} \gg N_0$ , when the crystals have intrinsic activity but introduced no noise. The ratio of the two  $\text{MDN}_0$  values, i.e. with crystal intrinsic activity to that without, is  $\sqrt{1 + N_{\text{LSO}}/N_0}$ . This can be translated for the estimation of the increased requirements for the MDTA with crystal intrinsic activity as compared to that without.

The ring artifacts from LSO activity estimation were effectively removed by the LSO correction method with the experimental hot-rod phantom study. This made SPECT imaging possible for image object with lower object activity levels or shorter acquisition time. This was particularly important for image planes acquired by the edge crystals of the detector blocks, where the LSO intrinsic activity level was higher and therefore had more severe impacts.

In the simulated studies (figures 8 and 9), a hot-ring artifact with a fixed diameter was observed. This corresponds to the edge crystals of the detector blocks along the axial direction.

The possible reason was the cropping of negative values after correcting the intrinsic activity when the object activity was low, which introduced a positive bias to the corrected projections. This artifact was not evident for the experimental studies (figures 7 and 10). It was probably the less than perfect system calibration that alleviated the effect of the bias introduced.

Based on the signal detectability in a projection bin, the cMDTA formula provided an estimate of the activity level and acquisition time required for obtaining images with good quality. The formula took into account the effects of image object's target size and background activity therefore it can be used in general imaging situations. One factor not included in the model was the number of projections or the angular sample size used in data acquisition. The number of projections for the phantom studies reported in this study was chosen so that the fine structure in the image object was adequately sampled. In addition, the signal and noise propagation of the image reconstruction algorithm was not considered in the cMDTA model. These missing components may have contributed to the consistent difference between eMDTA and cMDTA.

The SNR was effective in assessing the contrast phantom's image quality. However, it was not suitable for the hot-rod phantom images. The partial volume effect for the small rods made it difficult to define the ROIs and choose the SNR threshold for detectability. Having a recognizable hot-rod pattern in the 1.35 mm diameter section was used as the detectability measure in this work. A computer-observer-based detectability measure, e.g. a signal known exactly observer (Tapiovaara and Wagner 1993) for the expected image patterns shall facilitate the determination of a more accurate MDTA.

With the current 2D collimation configuration, the non-uniform pattern of intrinsic activity over crystals in a detector block (edge versus central) introduced varying image quality over different transverse planes. In order to achieve uniform image quality over axial direction, methods on addressing the non-uniform LSO distribution need to be studied.

Another way of reducing the effects of LSO intrinsic activity would be to increase the system sensitivity. While all the results presented used energy window 135–145 keV, studies using 120–160 keV energy window are expected to have lower cMDTA or yield better image with same acquisition configuration. However, the methodologies reported here will stand.

## 5. Conclusions

In summary, we implemented a simple LSO background subtraction method and demonstrated its effectiveness for SPECT imaging on a LSO-based animal PET scanner. The proposed projection-based MDTA calculation method takes into consideration LSO background, image target size and image target's background activity. For the four phantom studies evaluated, the cMDTA values were about five times of eMDTA values. For the proposed SPECT system, the LSO correction method is critical for quantitative and qualitative imaging and the MDTA calculation method may provide guidance in imaging protocol design and better understanding of imaging results.

## Acknowledgments

The authors would like to thank Dr Stefan Siegel of Siemens Preclinical Solutions for valuable assistance and discussions on the data acquisition; Central Radiopharmaceutical Service at SUNY Buffalo for providing radiopharmaceuticals for this study, and Mrs Rebecca Goodman for correcting the English of the manuscript. This work utilized the high-performance



computational capabilities of the Linux Cluster at the Center for Computational Research, State University of New York at Buffalo.

## References

- Barrett H H, Wilson D W and Tsui B M W 1994 Noise properties of the Em algorithm: 1. Theory *Phys. Med. Biol.* **39** 833–46
- Beekman F and Van Der Have F 2007 The pinhole: gateway to ultra-high-resolution three-dimensional radionuclide imaging *Eur. J. Nucl. Med. Mol. Imaging* **34** 151–61
- Budinger T F, Derenzo S E, Greenberg W L, Gullberg G T and Huesman R H 1978 Quantitative potentials of dynamic emission computed tomography *J. Nucl. Med.* **19** 309–15
- Frost & Sullivan 2006 *U.S. Preclinical Small Animal Imaging Markets Report* (Palo Alto: Frost & Sullivan)
- Goertzen A L, Suk J Y and Thompson C J 2007 Imaging of weak-source distributions in LSO-based small-animal PET scanners *J. Nucl. Med.* **48** 1692–9
- Huesman R H 1984 A new fast algorithm for the evaluation of regions of interest and statistical uncertainty in computed-tomography *Phys. Med. Biol.* **29** 543–52
- Jan S *et al* 2004 GATE: a simulation toolkit for PET and SPECT *Phys. Med. Biol.* **49** 4543–61
- Knoll G F 2000 *Radiation Detection and Measurement* (New York: Wiley)
- Laforest R, Longford D, Siegel S, Newport D F and Yap J 2007 Performance evaluation of the microPET (R) – FOCUS-F120 *IEEE Trans. Nucl. Sci.* **54** 42–9
- Lehnert W, Meikle S R, Siegel S, Newport D, Banati R B and Rosenfeld A B 2006 Evaluation of transmission methodology and attenuation correction for the microPET Focus 220 animal scanner *Phys. Med. Biol.* **51** 4003–16
- Ma T, Shao Y, Yao R and Manchiraju P 2007a Influence of PET down-scatter effect on SPECT imaging in PET and SPECT dual-tracer applications *IEEE Nuclear Science Symp. and Medical Imaging Conf. (Honolulu, Hawaii, USA, IEEE)* ed B Yu
- Ma T, Yao R and Shao Y 2007b Determination of geometrical parameters for slit-slat SPECT imaging on MicroPET *IEEE Nuclear Science Symp. and Medical Imaging Conf. (Honolulu, Hawaii, USA, IEEE)* ed B Yu
- Meikle S R, Kench P, Kassiou M and Banati R B 2005 Small animal SPECT and its place in the matrix of molecular imaging technologies *Phys. Med. Biol.* **50** R45–R61
- Qi J Y and Huesman R H 2006 Theoretical study of penalized-likelihood image reconstruction for region of interest quantification *IEEE Trans. Med. Imaging* **25** 640–8
- Schramm N U, Ebel G, Engeland U, Schurrat T, Behe M and Behr T M 2003 High-resolution SPECT using multipinhole collimation *IEEE Trans. Nucl. Sci.* **50** 315–20
- Shao Y, Yao R, Ma T, Luisi J C, Gao K, Balakrishna S and Li H 2006 Feasibility studies of a hybrid MicroPET and SPECT system for small animal imaging *IEEE Nuclear Science Symp. and Medical Imaging Conf. (San Diego, CA, USA, IEEE)* ed B Philips
- Shao Y, Yao R, Ma T and Manchiraju P 2007 Initial studies of PET and SPECT dual-tracer imaging with a MicroPET and an inserted collimator *IEEE Nuclear Science Symp. and Medical Imaging Conf. (Honolulu, Hawaii, USA, IEEE)* ed B Yu
- Santin G, Strul D, Lazaro D, Simon L, Krieguer M, Martins M V, Breton V and Morel C 2003 GATE: a Geant4-based simulation platform for PET and SPECT integrating movement and time management *IEEE Trans. Nucl. Sci.* **50** 1516–21
- Tapiovaara M J and Wagner R F 1993 Snr and noise measurements for medical imaging—Ia practical approach based on statistical decision-theory *Phys. Med. Biol.* **38** 71–92
- Watson C C, Casey M E, Eriksson L, Mulnix T, Adams D and Bendriem B 2004 NEMA NU 2 performance tests for scanners with intrinsic radioactivity *J. Nucl. Med.* **45** 822–6
- Wilson D W and Tsui B M W 1993 Noise properties of filtered-backprojection and ML-EM reconstructed emission tomographic-images *IEEE Trans. Nucl. Sci.* **40** 1198–203
- Wilson D W, Tsui B M W and Barrett H H 1994 Noise properties of the Em algorithm: 2. Monte-Carlo simulations *Phys. Med. Biol.* **39** 847–71
- Yao R, Ma T, Rathod V, Shao Y and Carson R E 2006 Deriving the system matrix of a slit-hole micro-SPECT system using Monte Carlo simulation *IEEE Nuclear Science Symp. and Medical Imaging Conf. (Honolulu, Hawaii, USA, IEEE)* ed B Philips